OPEN

A Green Strategy to Prepare Metal Oxide Superstructure from Metal-Organic Frameworks

Yonghai Song, Xia Li, Changting Wei, Jinying Fu, Fugang Xu, Hongliang Tan, Juan Tang & Li Wang

College of Chemistry and Chemical Engineering, Jiangxi Normal University, 99 Ziyang Road, Nanchang 330022, China.

Metal or metal oxides with diverse superstructures have become one of the most promising functional materials in sensor, catalysis, energy conversion, etc. In this work, a novel metal-organic frameworks (MOFs)-directed method to prepare metal or metal oxide superstructure was proposed. In this strategy, nodes (metal ions) in MOFs as precursors to form ordered building blocks which are spatially separated by organic linkers were transformed into metal oxide micro/nanostructure by a green method. Two kinds of Cu-MOFs which could reciprocally transform by changing solvent were prepared as a model to test the method. Two kinds of novel CuO with three-dimensional (3D) urchin-like and 3D rods-like superstructures composed of nanoparticles, nanowires and nanosheets were both obtained by immersing the corresponding Cu-MOFs into a NaOH solution. Based on the as-formed CuO superstructures, a novel and sensitive nonenzymatic glucose sensor was developed. The small size, hierarchical superstructures and large surface area of the resulted CuO superstructures eventually contribute to good electrocatalytic activity of the prepared sensor towards the oxidation of glucose. The proposed method of hierarchical superstructures preparation is simple, efficient, cheap and easy to mass production, which is obviously superior to pyrolysis. It might open up a new way for hierarchical superstructures preparation.

Metal or metal oxides with diverse micro/nanostructures have become one of the most promising functional materials in sensor, catalysis, energy conversion, etc, due to their superior chemical and physical properties, such as large specific surface area, high electronic conductivity, and good catalytic activity[1–4]. Up to now, numerous well-defined micro/nanostructured metal oxide (such as nanoparticles, nanotubes, nanosheets, nanowires, etc) have been synthesized[5,6]. And the research on micro/nanostructures has been recently expanded to the assembly of low-dimensional nanoscaled building blocks into unprecedented three-dimensional (3D) hierarchical superstructures[7,8]. Typically, there are two strategies to construct hierarchical superstructures: One is "bottom-up" route[9], which has been widely applied in recent years. And it means fabricating hierarchical superstructures from basic building block. The other is "top-down" approach[10], which means producing superstructures by decomposing large materials. Since the common top-down method (optical lithography, electron beam lithography) has high requirements on experiment condition including clean room, vacuum, etc, the solution-based "bottom-up" approach, which is low-cost and high efficient, is considered more promising in precise nanofabrication.

Metal-organic frameworks (MOFs) built from metal ions (or clusters) and organic bridging ligands through strong coordination bonds have recently received increased attention as hybrid materials[11]. They have emerged as interesting functional materials due to their tunable structures with high thermal stability, organic functionality, large pore sizes, open metal sites in the skeleton and high surface areas[12,13]. A wide range of applications including heterogenous catalysis, gas storage and adsorption, drug delivery and release, multimodal imaging and sensing have been reported[14–19]. Recently, it has been the focus of intense research interest because MOFs can act as precursors to prepare metal or metal oxide hierarchical superstructures by pyrolysis[20–23]. For example, Yang et al. reported the one-step themolysis of IRMOF-1 to prepare porous carbon-coated ZnO quantum dots as an anode material in lithium ion batteries[24]. Das et al. explored the preparation of metal and metal oxides hierarchical superstructures by using MOFs in detail[25]. As pyrolysis of MOFs has been widely explored, it is known to be a convenient way to construct metal or metal oxides superstructures[26]. However, it has not taken full advantage of various MOFs unique structure because different MOFs always result in analogous superstructures. Besides, metal or metal oxides tend to aggregate and lose their hierarchical superstructures in pyrolysis process[27].

Therefore, other green strategies to fabricate metal or metal oxide hierarchical superstructures based on MOFs still need to be explored[28].

In this work, two kinds of Cu-MOFs which could reciprocally transform by changing solvent were prepared. Two kinds of corresponding novel CuO with three-dimensional (3D) urchin-like superstructures and 3D rods-like superstructures composed of nanoparticles, nanowires and nanosheets were obtained by immersing the above Cu-MOFs in NaOH solution. Unlike pyrolysis which is inefficient, energy consumption and environmentally hazardous, this route is green and environmentally friendly. A superior application of the as-prepared CuO superstructures in electrochemical detection of glucose was also investigated.

Results and Discussion

Two kinds of Cu-BTC have been successfully prepared according to modified hydrothermal methods[29]. The scanning electron microscope (SEM) images show the clear shape of Cu-BTC (Fig. 1A and B). One is typically octahedral shape (Fig. 1A), and the other is firstly identified as rod-like crystals (Fig. 1B) and further confirmed as six-prismatic crystals by the high-magnified image (inset in Fig. 1B). The size of the crystals would change with the increase of nucleation time. From the XRD patterns, the octahedral crystals was confirmed to be of the well-known HKUST-1 (curve a in Fig. 1E) and the six-prismatic crystals was of catena-triaqua-mu-(BTC)-Cu (curve a in Fig. 1F)[29]. Fig. 1G shows the FTIR spectrum of both configurations of Cu-BTC. The broad absorption band near 3500 cm^{-1} is due to the coordinated water in the materials. The characteristic bands around 1600 and 1400 cm^{-1} are assigned to the symmetric and asymmetric stretching vibration of the -COO⁻ groups of the ionized ligand, respectively[30]. By contrast, two additional peaks appear at 1710 and 1242 cm^{-1} in FTIR spectrum of six-prismatic crystals (Fig. 1G(b)), indicating the presence of carboxylic acid group. These results suggested that BTC group only partially participates in the coordination in six-prismatic crystals[31]. Unlike the symmetrical dimeric copper (II) carboxylate type of structural units found in

octahedral crystals, the coordination of the carboxylic acid to metal ions is rather unsymmetrical in the six-prismatic crystal. Both kinds of Cu-BTC were further characterized with thermogravimetric analysis (TGA) in N_2 gas, as shown in curve a and b in Fig. 1H. For six-prismatic crystals (curve b), it shows a loss of 17% due to coordinated water vapor at 220°C, roughly corresponding to three water molecules per formular unit. For octahedral crystal, there is a continuous weight loss (27%) at low temperature (<100°C). Note that the first step in octahedral crystal is associated with the loss of physisorbed water and its exact amount depends on the initial hydration degree of the material.

In this work, an interesting phenomenon was observed that the six-prismatic crystals could convert into the octahedral crystals by changing solvent. After the six-prismatic crystals were immersed in an alcohol-water (4 : 1) solvent at 75°C for 8 days, they could transform into octahedral crystals. Fig. 1C shows a typical SEM image of the transformed octahedral crystals. A large number of nanoparticles with blurry octahedral shape and several bigger ones with clear octahedral shape with a diameter below 2 μm were observed. They are much smaller than those directly synthesized ones with size from 1 μm to 10 μm. Fig. 1E (b) shows its corresponding XRD patterns. All of these diffraction peaks could also be indexed to crystalline HKUST-1 and no obvious peaks of impurities was detected. As for these as-synthesized octahedral crystals, besides the diffraction peaks belong to crystalline HKUST-1, some impurities peaks have been detected. Therefore, the transformation from six-prismatic crystals to octahedral crystals could be realized.

Similarly, the transformation from octahedral crystal to rod-like crystals could also been realized by changing solvent[32]. Fig. 1D shows the SEM image of the crystal prepared by immersing the octahedral crystals in ultra-pure water for 1 day. It was observed that rod-like crystals has been formed at a large scale. There were some subtle differences from directly synthesized ones. Rod-like crystals transformed from octahedral crystals had not the typical hexagonal cross section as the six-prismatic crystals. XRD was used to study the difference between the rod-like structures and the six-prismatic crystals.
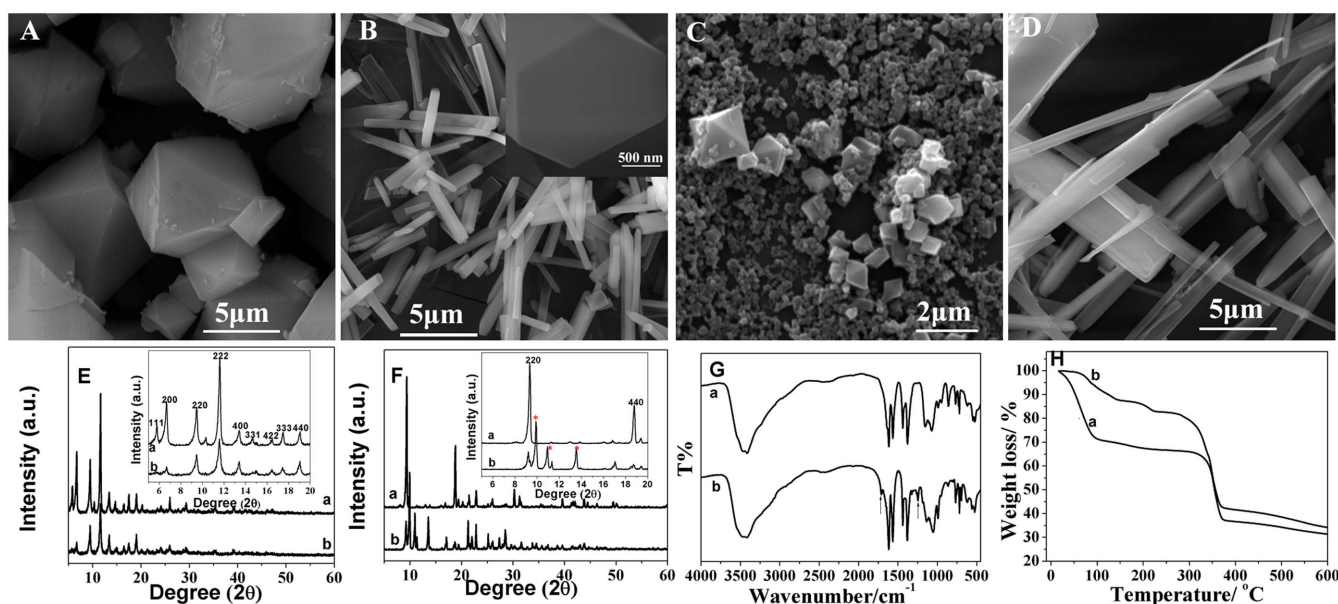

Figure 1 | SEM images of octahedral (A) and six-prismatic (B) Cu-MOFs, octahedral Cu-MOFs transformed from six-prismatic Cu-MOFs (C), and six-prismatic Cu-MOFs transformed from octahedral Cu-MOFs (D). Inset B: high-resolution image. (E) XRD of octahedral Cu-MOFs (curve a) and octahedral Cu-MOFs transformed from six-prismatic Cu-MOFs (curve b). (F) XRD of six-prismatic Cu-MOFs (curve a) and six-prismatic Cu-MOFs transformed from octahedral Cu-MOFs (curve b). Inset in C and D: local amplification of 2θ from 5–20 degree. The red * show the additional peaks in six-prismatic crystals transformed from octahedral Cu-MOFs. (G) FTIR of octahedral (curve a) and six-prismatic (curve b) Cu-MOFs. The arrows point towards the additional peaks in six-prismatic crystals. (H) TGA curves of octahedral (curve a) and six-prismatic (curve b) Cu-MOFs.

Unlike six-prismatic crystals which is highly oriented along the [220] direction, only a part of rod-like crystals oriented along the [220] as shown in Fig. 1F (b). Besides, several additional characteristic diffraction peaks appear as marked by stars, indicating an unknown phase appeared.

The above results clearly demonstrate that the two different configurations of Cu-BTC materials could realize quasi-reversible structural transformation. Although the octahedral crystals could not completely transform into six-prismatic crystals, it could transform into clavate crystals. It is believed that octahedral crystals possess Cu_2-paddle-wheel unit and the residual axial coordination site is filled by two water molecules with weak binding. While in six-prismatic crystal, the Cu atoms show a distorted pyramidal coordination geometry involving two carboxylic O atoms and three water molecules[33,34]. We speculate that the water content in mother solution influences the coordinate mode of Cu atom and further influences the crystal growth direction. However, the detailed transformation mechanism is still unknown.

CuO is an important transition metal oxide with a narrow band gap and has been widely used in sensor, optics, electronics, catalytic, and solar cell[35–38]. Up to now, only a few CuO superstructures have been obtained, such as "dandelions", "honeycombs", "hollow microspheres", etc[39–42]. Herein, two kinds of novel CuO with 3D urchin-like superstructures and 3D rod-like superstructures composed of nanoparticles, nanowires and nanosheets were obtained by immersing the corresponding Cu-MOFs into NaOH solution. The typical morphology of CuO hierarchical superstructures obtained from octahedral crystal is shown in Fig. 2. As shown by low-magnified SEM image (Fig. 2A), the CuO presents uniform urchin-like structure at a large scale with diameters around 10 μm. In the middle of each urchin, it seems retain octahedral shape. High-resolution SEM image (Fig. 2B) shows that the spike of 3D urchin was composed of a large number of nanosheets. Higher-magnified SEM image (inset in Fig. 2B) shows that some tiny nanoparticles with an average size of 25 nm first formed nanowires by "head-to-head" connection, then these nanowires further formed 2D corn husks-like nanosheets by "shoulder-to-shoulder" oriented attachment. The corn husks-like nanosheets with a width ranging from c.a. 100 nm in tail to 1 μm in root and radiate from the center of octahedron to make up each 3D urchin-like CuO hierarchical superstructures. To determine its phase purity, typical XRD pattern was carried out and the result was shown in Fig. 2C. As marked by blue label, the peaks at 32°, 35°, 39°, 49°, 53° and 58° can be easily indexed to (110), (111), (111), (202), (020) and (202) crystal plane of monoclinic-phase CuO (JCPDS Card No. 45-937). In addition, the peaks at 0–30° can be assigned to octahedral crystal of Cu-BTC, suggesting that the Cu-BTC could not transform into CuO superstructures completely in a short time. The products of octahedral Cu-MOFs immersed in 0.1 M NaOH for 1 h, 5 h, 12 h and 24 h were characterized with TGA. As shown in Fig. 2D, the complexes synthesized by alkali treatment for 1 h and 5 h showed two weight loss stages. The first stage is corresponding to the departure of absorbed water molecules (<300°C according to Fig. 1H) and the second stage is attributable to decomposition of the organic ligands (>300°C according to Fig. 1H). The gradient of the second weight loss stage decreased gradually with the increase of immersion time, indicating the decrease of organic ligands. The second stage wasn't observed in the curve of materials synthesized by alkali treatment for 12 h and 24 h revealing complete transformation from Cu-BTC crystals to CuO and there was no organic residue.

Unlike the transformation from octahedral crystal to urchin-like CuO superstructures, the rod-like shape of six-prismatic crystals was kept after six-prismatic crystals was immersed into NaOH solution (Fig. 3A). As indicated by the magnified SEM image (Fig. 3B), the rod-like structure was composed of many plate-like units. The inset
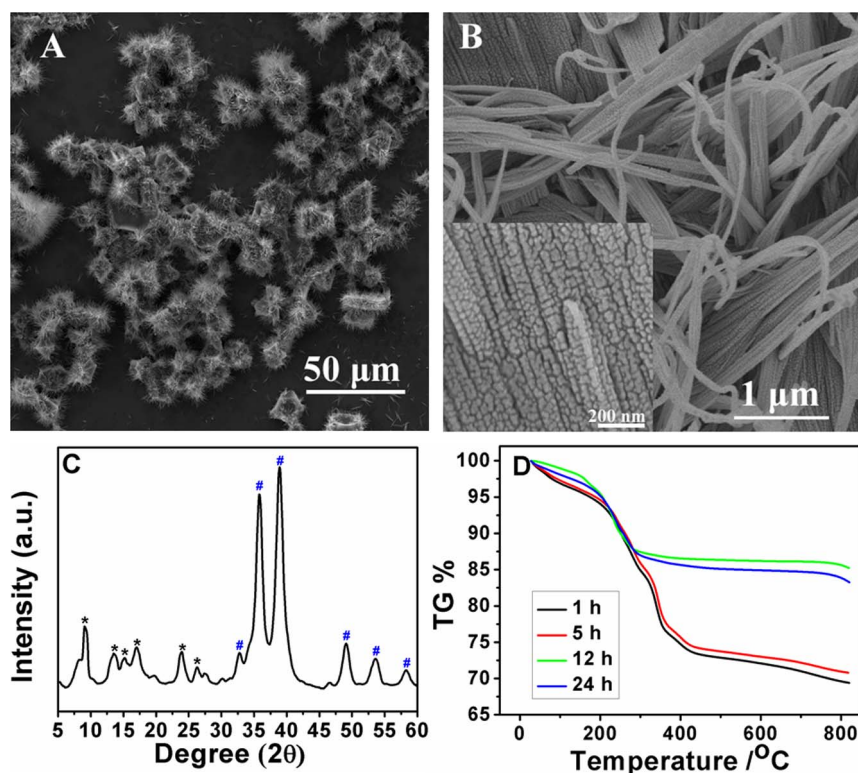

Figure 2 | Low-magnification SEM image (A) and high-magnification SEM image (B) of CuO superstructure prepared by immersing octahedral Cu-MOFs in 0.1 M NaOH for 72 h. Inset in B: partial enlargement. (C) XRD of the octahedral Cu-MOFs immersed in 0.1 M NaOH for 72 h. The * and # show the diffraction peaks of octahedral Cu-MOFs and CuO, respectively. (D) TGA curves of complexes synthesized by immersing octahedral Cu-MOFs in 0.1 M NaOH for 1 h, 5 h, 12 h and 24 h.
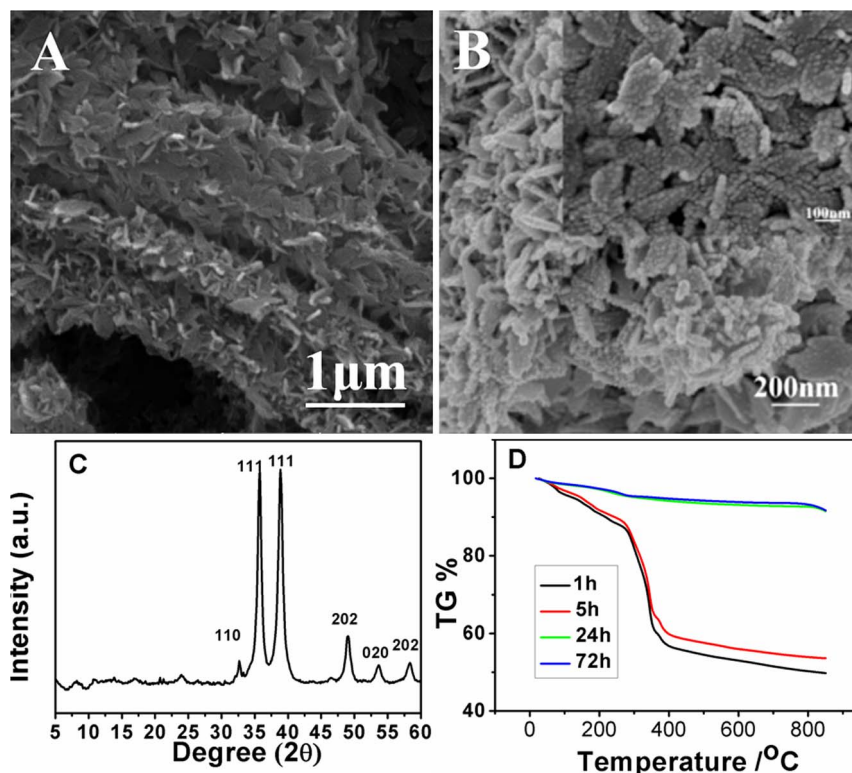
Figure 3 | Low-magnification SEM image (A) and high-magnification SEM image (B) of CuO superstructure prepared by immersing six-prismatic Cu-MOFs in 0.1 M NaOH for 72 h. Inset in B: partial enlargement. (C) XRD of the six-prismatic Cu-MOFs immersed in 0.1 M NaOH for 72 h. (D) TGA curves of complexes synthesized by immersing six-prismatic Cu-MOFs in 0.1 M NaOH for 1 h, 5 h, 12 h and 24 h.

in Fig. 3B demonstrates that the plate-like units were composed of many tiny nanoparticles with a few ten nanometers in diameter. Consequently, the CuO superstructures have three-order hierarchy: nanoparticles, nanoplates and rods. As disclosed by XRD (Fig. 3C), the sharp diffraction peaks at 2θ angles of 32°, 35°, 39°, 49°, 53° and 58° corresponded to (110), (111), (111), (202), (020), (202) crystal plane of monoclinic-phase CuO (JCPDS Card No. 45-937), respectively. And the diffraction of the six-prismatic crystals was hardly detectable. It suggested that most six-prismatic crystals have transformed into rod-like CuO superstructures. Furthermore, the thermal stability of rod-like CuO superstructures was also tested and the result was shown in Fig. 3D. Weight loss of 44% and 41% were observed in the TGA test of incompletely conversed six-prismatic

Cu-MOFs (1 h and 5 h) at the second stage. There was only 5% weight loss in the stage of absorbed water molecules departure for rod-like CuO superstructures (24 h and 72 h) while the weight loss of six-prismatic crystals was as high as 12.5%. The well thermal stability of the rod-like CuO superstructures revealed complete transformation from Cu-BTC crystals to CuO and there was no organic residues remained.

Time-dependent morphology evolution study was performed to thoroughly understand the superstructures formation process. At the early stage when the octahedral crystal was immersed into NaOH solution, the rapid nucleation of nanoparticles made the smooth surface rough quickly, as shown in Fig. 4A and E–H. After 2 h, it was hard to identify a clear octahedral shape, but it looked more like a
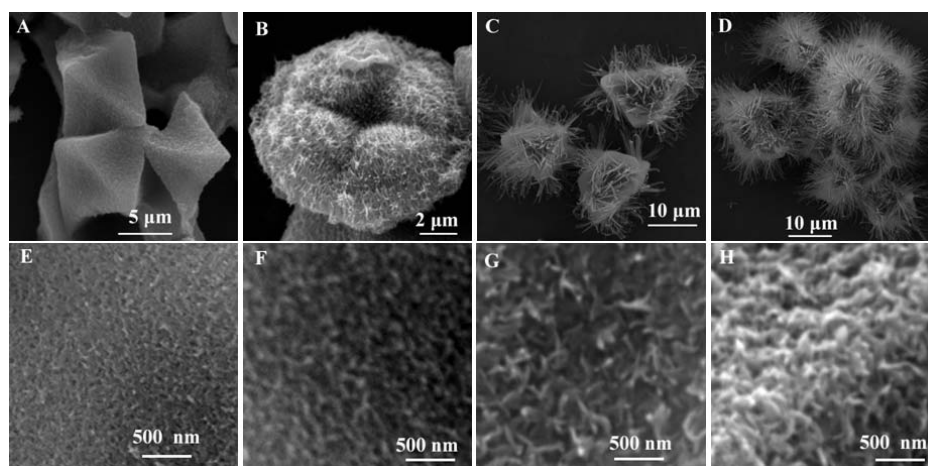

Figure 4 | SEM images of CuO superstructure prepared by immersing octahedral Cu-MOFs in 0.1 M NaOH for different time at room temperature: (A) 1 h, (B) 2 h, (C) 5 h, (D) 12 h, and high-magnification SEM images for different time: (E) 10 min, (F) 20 min, (G) 30 min and (H) 1 h.
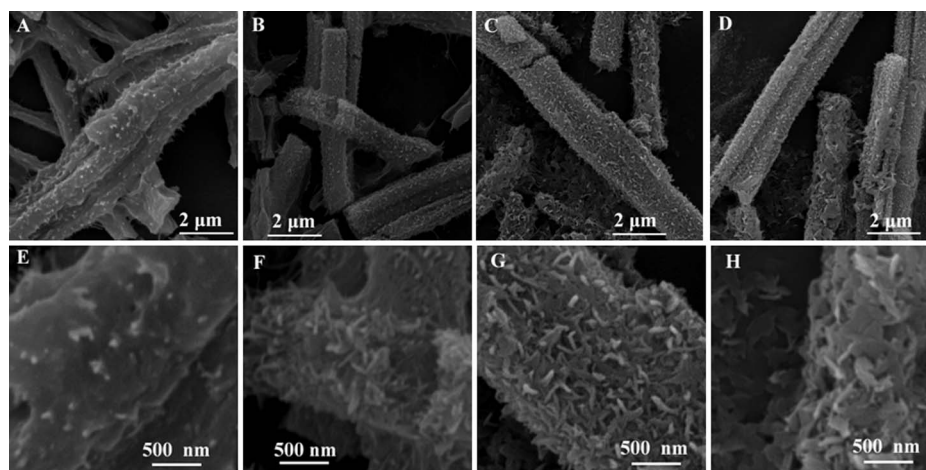
Figure 5 | SEM images of CuO superstructure prepared by immersing six-prismatic Cu-MOFs in 0.1 M NaOH for different time at room temperature: (A) 5 min, (B) 10 min, (C) 30 min and (D) 5 h. Corresponding high-magnification images were shown in (E), (F), (G) and (H).

hair bulb with dense nanowires and nanosheets outside (Fig. 4B). As the immersing time prolonged, moiety of nanosheets formed by nanowires began to appear and eventually the residual octahedral centre was wrapped up by dense nanosheets to produce urchin-like CuO superstructures (Fig. 4C and D). Fig. 5 shows the process of transformation from six-prismatic crystals to the rod-like CuO superstructures in details. Similar to the process that octahedral crystals converted into urchin-like CuO superstructure, the rod-like CuO superstructures also experienced the formation of nanoparticles (Fig. 5A–F), then transformation from nanoparticles to nanoplates (Fig. 5E–G), eventually a myriad of nanoplates gather and grow into the rod-like CuO superstructures.

The reason that octahedral crystal transformed into urchin-like CuO superstructure while six-prismatic crystals turned into rod-like CuO superstructure could be interpreted as the difference from internal coordination mode. When the Cu-BTC was immersed into NaOH solution, reaction occurs according to the following steps[43,44]:

$$Cu\text{-}BTC + NaOH \rightarrow Cu(OH)_2 \tag{1}$$

$$Cu(OH)_2 \rightarrow CuO + H_2O \tag{2}$$
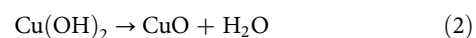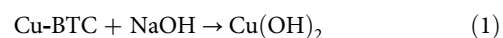
For octahedral crystals, Cu_2-clusters are connected with four carboxylate groups to give a paddle-wheel unit as shown in Fig. 6[33]. The short Cu-Cu internuclear separation of 0.26 nm is reasonable for CuO nanoparticles to connect into nanowires. From the view inside the pore (Fig. 6), the axis of Cu_2-clusters point towards the pore center makes it easy to form urchin-like structure that radiate outside from the centre. On the other hand, owing to MOFs' infinite ordered arrangement, these paralleled CuO nanowires further assemble into nanosheets and eventually form 3D urchin-like superstructures. While, in six-prismatic crystals, two of the three carboxylic groups of the acid are used as ligands to Cu atoms, bridging them to give polymeric zigzag chains. Such zigzag chains are connected into
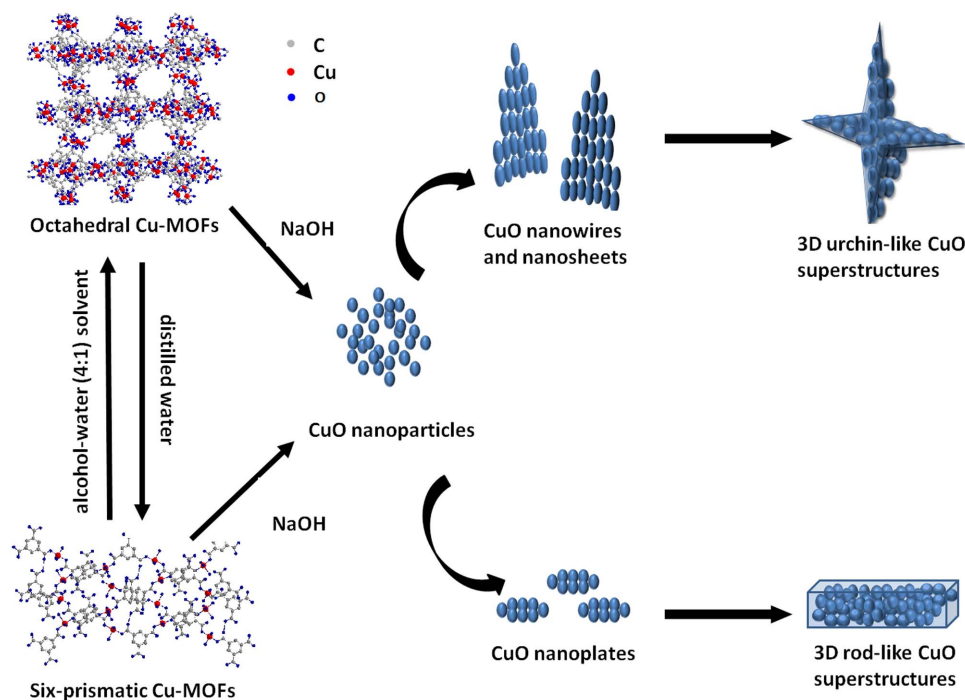

Figure 6 | Schematic illustration of the formation process of hierarchical CuO superstructure from two kinds of Cu-MOFs.
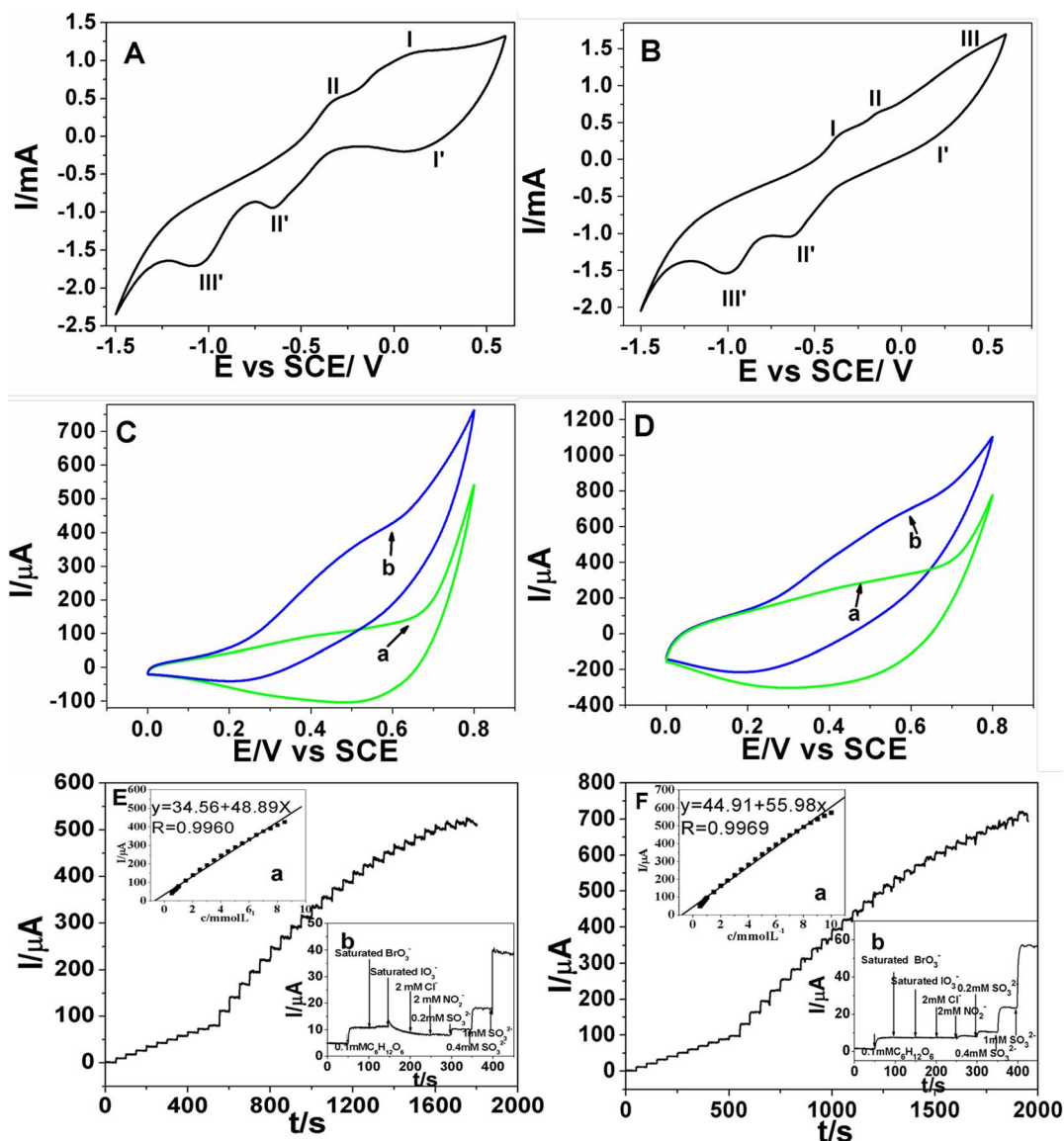
Figure 7 | CVs of urchin-like CuO superstructure/CPE (A) and rod-like CuO superstructure/CPE (B) in 0.1 M NaOH at 100 mV s^{-1}. CVs of urchin-like CuO superstructure/CPE (C) and rod-like CuO superstructure/CPE (D) in the absence (curve a) and presence (curve b) of 5.0 mM glucose in 0.10 M NaOH at 50 mV s^{-1}. Typical amperometric response of urchin-like CuO superstructure/CPE (E) and rod-like CuO superstructure/CPE (F) to successive injection of glucose into the stirred 0.10 M NaOH. Insets in E and F: (a) the corresponding calibration curve and (b) interference testing. Applied potential: (E) 0.60 V and (F) 0.55 V. $m_{Cu-MOFs}/m_{graphite} = 1:10$.

sheets via hydrogen bonds, and neighboring sheets are connected each other via hydrogen bonds too (Fig. 6)[34]. The zigzag chains nature makes the produced nanoparticles hard to form nanowires while easy to gather into nanosheets. Thanks to the slender shape of six-prismatic crystals itself, it transform completely into rod-like CuO superstructure. Furthermore, from the thermodynamic viewpoint, the bigger particles grown from small primary nanoparticles through an oriented attachment mechanism are driven by the force to eliminate the high energy surfaces[45].

Nitrogen adsorption–desorption isotherms were measured to evaluate the surface area and the pore size distribution of CuO superstructure and the results were shown in Fig. S2A. The tails steeply increased at the relative pressure near to 1.0 revealed the presence of macroporosity. The majority of pores are located in the region of mesopore. Both the samples display average pore size distribution at ca. 20.0 nm as shown in the pore size distributions curve calculated from the nitrogen adsorption branches (Fig. S2B). The BET surface area of the urchin-like CuO and rod-like CuO is 20.5 m^2 g^{-1} and

40.6 m^2 g^{-1}, respectively, both are higher than that of most reported CuO nanostructures[46–48]. Those nanostructures interweave together to form an open porous structure and are expected to facilitate electrolyte penetration into the electrode particles, thus providing more active sites.

The nonenzymatic glucose sensors are developed based on both CuO superstructures. Firstly, the electrochemical behaviors of CuO superstructure/carbon paste electrode (CPE) were both investigated by CVs in 0.1 M NaOH solution as shown in Fig. 7. In Fig. 7A, there are two anodic peaks (peaks I and II) and three cathodic peaks (peaks I′, II′ and III) in the scanning potential range. The cathodic peaks at 0.2 V (peak I') and −0.65 V (peak II′) are attributed to the reduction of Cu^{2+}→Cu$^+$ and Cu$^+$→Cu, respectively. While the anodic peaks at −0.35 V (peak II) and −0.2 V to 0 V (peak I) are attributed to the oxidation of Cu→Cu$^+$ and Cu$^+$→Cu^{2+}, respectively[49]. The cathodic peak around −1.0 V (peak III) is due to the reduction of soluble O$_2$. In Fig. 7B, the result is similar to that in Fig. 7A except the peak potential shows a little deviation.

The electrocatalytic activities of both CuO superstructure/CPEs toward the oxidation of glucose have also been investigated in 0.1 M NaOH (Fig.7C and D). When 1.0 mM glucose was added into electrolyte, both sensors exhibited a remarkable catalytic current beyond 300 µA at 0.50–0.60 V (curve b). The current might result from the electrocatalytic oxidation of glucose by Cu^{3+} species as compared with that in the absence of glucose (curve a). The catalytic mechanism for glucose oxidation might be as following: Cu^{2+} species was firstly oxidized to Cu^{3+} species in higher potential then glucose was oxidized by Cu^{3+} species, which resulted in the regeneration of Cu^{2+} species. According to the above CV results, the possible redox mechanism could be assumed as follows:

$$2CuO + H_2O \rightarrow 2CuOOH \qquad (3)$$

$$2CuOOH + glucose \rightarrow 2CuO + 2H_2O + gluconolactone \quad (4)$$
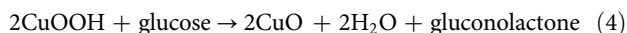
This result provides the first evidence that both novel CuO superstructures have good electrocatalytic ability towards glucose oxidation, which could be attributed to their small particle size and large enough surface area.

The mass ratio of CuO to graphite ($m_{CuO}/m_{graphite}$) in the preparing process of CuO superstructure CPE was optimized as shown in Fig. S1. The mass ratio of 1 : 10 was chosen as the optimum ratio and used to prepare electrodes for further investigation. Amperometric measurements were carried out at 0.60 V and 0.55 V for the urchin-like (Fig. 7E) and the rod-like (Fig. 7F) CuO superstructure/CPE by successive injection of glucose into a stirring 0.1 M NaOH, respectively. The oxidation current on urchin-like CuO superstructure/CPE reached a maximum steady-state value within 5 s. The oxidation current was proportional to glucose concentration in the range of 0.5–8.5 mM (r = 0.9960) with a slope of 48.89 µA mM^{-1} (inset a in Fig. 7E). The detection limit was estimated to be 43 µM based on the criterion of a signal-to-noise ratio of 3. Similarly, the linear range of glucose detection on the rod-like CuO superstructure/CPE was determined to be from 0.5 mM to 10 mM (r = 0.9969) with a slope of 55.98 µA mM^{-1}, and the detection limit was estimated to be 77 µM (inset a in Fig. 7F). The performance of our sensor and those reported in literature work regarding the performance of glucose assay were summarized in Table 1[50,51]. While glucose sensors based on glucose oxidase have made good progress, here we only list the sensors based on inorganic materials for comparison[52,53]. It indicates that our sensors have better catalytic activity and sensitivity towards the oxidation of glucose, which might results from the small size nature and large surface area of as-formed CuO superstructures.

Since some easily oxidative species always coexisted with glucose, interference test was also investigated here as shown by inset b in Fig. 7E and 7F. For the CuO superstructure/CPE, chemicals such as saturated BrO_3^-, 20-fold concentration of Cl^- and NO_2^- showed no interference for the determination of glucose. While saturated IO_3^- and 2-fold concentration of SO_3^{2-} showed obvious interference to the oxidation of glucose.

The stability, repeatability and reproducibility of both sensors were also investigated. After the CuO superstructure/CPE was stored at room temperature for two weeks, the current response to 0.1 mM glucose only decreased by 3.21% and 7.04% for the urchin-like and the rod-like CuO superstructure/CPE, respectively. The repeatability of successive amperometric measurements of 0.1 mM glucose for 4 times was carried out. A relative standard deviation values (RSD) of 4.75% and 2.63% were calculated for the urchin-like and the rod-like CuO superstructure/CPE, respectively. The reproducibility of the response to 0.1 mM glucose obtained with five different sensors was also evaluated with a RSD of 4.05% and 3.05% for the urchin-like and the rod-like CuO superstructure/CPE, respectively.

In summary, this study provides a novel green route to synthesize novel metal oxide superstructures from MOFs. Two kinds of CuO hierarchical superstructures have been synthesized based on two

different configurations of Cu-BTC materials. Because of the small size and high surface area of the resulted CuO superstructures, the final products exhibit an excellent and stable electrocatalytic activity toward the electrochemical oxidation of glucose. The inner structure of MOFs plays a key role in controlling the hierarchical superstructures of the prepared CuO. Due to the structural diversity of MOFs, the proposed approach could be extended for the preparation of other metal oxide with a number of potential applications.

Methods

Materials. Graphite powder, liquid paraffin, and d(+)-glucose was purchased from Aladdin. 1,3,5-Benzentricarboxylic acid (BTC) was obtained from the Sigma-Aldrich (Milwaukee Wisconsin). $Cu(NO_3)_2 \cdot 3H_2O$, absolute ethanol and other reagents were purchased from Beijing Chemical Reagent Factory (Beijing, China). All reagents were of analytical grade and used without further purification. All solutions were prepared with ultra-pure water, purified by a Millipore-Q system (18.2 MΩ cm).

Instrumentation. The scanning electron microscopy (SEM) analysis was taken using a XL30 ESEM-FEG SEM at an accelerating voltage of 20 kV equipped with a Phoenix energy dispersive x-ray analyzer (EDXA). The samples for SEM observation were prepared by placing 10 µL Cu-BTC suspension on a silicon surface, followed by drying at room temperature. X-ray powder diffraction (XRD) data were collected on a D/Max 2500 V/PC X-ray powder diffractometer using Cu Kα radiation (λ = 0.154056 nm, 40 kV, 200 mA). Fourier transform infrared spectra (FTIR) were recorded on a Nicolet 6700 FTIR spectrophotometer. Thermogravimetric analysis (TGA) was carried out with a SDT 2960 Simultaneous DSC-TGA, TA Instrument. All electrochemical measurements were performed on a CHI 660C electrochemical workstation (Shanghai, China) at ambient temperature. A conventional three-electrode system was employed including two kinds of CuO/CPE as working electrode, a platinum wire as auxiliary electrode and a SCE saturated KCl as reference electrode. The cyclic voltammetric experiments were performed in a quiescent solution. The amperometric experiments were carried out under a continuous stirring. 0.1 M NaOH as the supporting electrolyte solution was purged with high purity nitrogen for 15 min prior to each measurement and a nitrogen atmosphere was kept over the solution during measurements.

Synthesis of Two Kinds of Cu-BTC. Octahedral Cu-BTC was synthesized by solvothermal method. Typically, 8 mL 0.35 mol/L $Cu(NO_3)_2$ aqueous solution and 24 mL 0.10 mol/L BTC ethanol solution was stirred by magnetic for 10 min. Then the suspension was filled into a Teflon container and placed into an autoclave, and left for 8 days in a preheated oven at 75°C. After the synthesis mixture in a water/ice bath was cooled, the crystalline product was filtrated and washed with a mixed alcohol-water (1 : 1) solution and dried at 100°C for 12 h. The six-prismatic crystal was prepared by the same procedure expect the suspension contained 17.5 mL 0.10 mol/L $Cu(NO_3)_2$ aqueous solution and 12 mL 0.20 mol/L BTC ethanol solution.

Preparation of CuO Hierarchical Superstructure. 1.0 g of the prepared Cu-BTC was immersed into 50 mL 0.1 M NaOH solution. Then magnetic stirring was employed to ensure sufficient reaction between Cu-BTC and NaOH. When reactions were accomplished, the product was isolated by filtering, and washed thoroughly with distilled water to give CuO superstructure.

Preparation of the CuO Superstructure/CPE. The CuO hierarchical superstructure/CPE was prepared as follows. Graphite powder and CuO hierarchical superstructure were mixed in different ratio, and several drops of liquid paraffin was added. After it was carefully grinded in an agate mortar for 20 min, a homogenized paste was formed. The homogenized mixture was packed firmly into a clean and dry glass tube (5 mm in inner diameter and 1.0 cm in length). The electrical contact was established with a copper wire connected to the paste. After natural drying at room temperature, the surface of the electrode was smoothed by lightly friction on the weighing paper before use. This procedure could also used to regenerate the surface of the CuO hierarchical superstructure/CPE.

1. Hahn, Y. B., Ahmad, R. & Tripathy, N. Chemical and biological sensors based on metal oxide nanostructures. *Chem. Commun. (Camb)* **48**, 10369–10385 (2012).
2. Xu, H., Zhu, G., Zheng, D., Xi, C., Xu, X. & Shen, X. Porous CuO superstructure: Precursor-mediated fabrication, gas sensing and photocatalytic properties. *J. Colloid Interface Sci.* **383**, 75–81 (2012).
3. Ko, S., Lee, J.-I., Yang, H. S., Park, S. & Jeong, U. Mesoporous CuO Particles Threaded with CNTs for High-Performance Lithium-Ion Battery Anodes. *Adv. Mater.* **24**, 4451–4456 (2012).
4. Wang, G., Zhang, L. & Zhang, J. A review of electrode materials for electrochemical supercapacitors. *Chem. Soc. Rev.* **41**, 797–828 (2012).
5. Lignier, P., Bellabarba, R. & Tooze, R. P. Scalable strategies for the synthesis of well-defined copper metal and oxide nanocrystals. *Chem. Soc. Rev.* **41**, 1708–1720 (2012).
6. Oh, M. H. *et al.* Galvanic Replacement reactions in metal oxide nanocrystals. *Science* **340**, 964–968 (2013).

7. Cölfen, H. & Antonietti, M. Mesocrystals: inorganic superstructures made by highly parallel crystallization and controlled alignment. *Angew. Chem. Int. Ed.* **44**, 5576–5591 (2005).

8. Suresh, V., Madapusi, S. & Krishnamoorthy, S. Hierarchically built hetero-superstructure arrays with structurally controlled material compositions. *ACS Nano* **7**, 7513–7523 (2013).

9. Ozin, G. A. *et al.* Nanofabrication by self-assembly. *Mater. Today* **12**, 12–23 (2009).

10. Yang, J. *et al.* A top-down strategy towards monodisperse colloidal lead sulphide quantum dots. *Nat. Commun.* **4**, 1695 (2013).

11. Stock, N. & Biswas, S. Synthesis of metal-organic frameworks (MOFs): routes to various MOF topologies, morphologies, and composites. *Chem. Rev.* **112**, 933–969 (2012).

12. Cheng, Y. *et al.* Reversible structural change of Cu-MOF on exposure to water and its CO_2 adsorptivity. *Langmuir* **25**, 4510–4513 (2009).

13. Jeong, E. *et al.* Reversible structural transformation and selective gas adsorption in a unique aqua-bridged Mn(II) metal-organic framework. *Chem. Commun. (Camb)* **49**, 2329–2331 (2013).

14. Herm, Z. R. *et al.* Separation of hexane isomers in a metal-organic framework with triangular channels. *Science* **340**, 960–964 (2013).

15. Zhu, X. *et al.* Metal-organic framework (MOF): a novel sensing platform for biomolecules. *Chem. Commun. (Camb)* **49**, 1276–1278 (2013).

16. Hartmann, M. *et al.* Adsorptive separation of isobutene and isobutane on $Cu_3(BTC)_2$. *Langmuir* **24**, 8634–8642 (2008).

17. Dhakshinamoorthy, A. & Garcia, H. Catalysis by metal nanoparticles embedded on metal-organic frameworks. *Chem. Soc. Rev.* **41**, 5262–5284 (2012).

18. Kreno, L. E. *et al.* Metal-organic framework materials as chemical sensors. *Chem. Rev.* **112**, 1105–1125 (2012).

19. Morozan, A. & Jaouen, F. Metal organic frameworks for electrochemical applications. *Energ. Environ. Sci.* **5**, 9269–9290 (2012).

20. Liu, B., Shioyama, H., Akita, T. & Xu. Q, Metal-organic framework as a template for porous carbon synthesis. *J. Am. Chem. Soc.* **130**, 5390–5391 (2008).

21. Kim, T. K. *et al.* Nanoporous metal oxides with tunable and nanocrystalline frameworks via conversion of metal-organic frameworks. *J. Am. Chem. Soc.* **135**, 8940–8946 (2013).

22. Xi, K. *et al.* Carbon with hierarchical pores from carbonized metal-organic frameworks for lithium sulphur batteries. *Chem. Commun. (Camb)* **49**, 2192–2194 (2013).

23. Torad, N. L. *et al.* Facile synthesis of nanoporous carbons with controlled particle sizes by direct carbonization of monodispersed ZIF-8 crystals. *Chem. Commun. (Camb)* **49**, 2521–2523 (2013).

24. Yang, S. J. *et al.* Preparation and exceptional lithium anodic performance of porous carbon-coated ZnO quantum dots derived from a metal-organic framework. *J. Am. Chem. Soc.* **135**, 7394–7397 (2013).

25. Das, R., Pachfule, P., Banerjee, R. & Poddar, P. Metal and metal oxide nanoparticle synthesis from metal organic frameworks (MOFs): finding the border of metal and metal oxides. *Nanoscale* **4**, 591–599 (2012).

26. Jung, S., Cho, W., Lee, H. J. & Oh, M. Self-template-directed formation of coordination-polymer hexagonal tubes and rings, and their calcination to ZnO rings. *Angew. Chem. Int. Edit.* **48**, 1459–1462 (2009).

27. Liu, B. *et al.* Converting cobalt oxide subunits in cobalt metal-organic framework into agglomerated Co_3O_4 nanoparticles as an electrode material for lithium ion battery. *J. Power Sources* **195**, 857–861 (2010).

28. Zhang, L., Wu, H. B. & Lou, X. W. Metal-organic-frameworks-derived general formation of hollow structures with high complexity. *J. Am. Chem. Soc.* **135**, 10664–10672 (2013).

29. Schlichte, K., Kratzke, T. & Kaskel, S. Improved synthesis, thermal stability and catalytic properties of the metal-organic framework compound $Cu_3(BTC)_2$. *Micropor. Mesopor. Mat.* **73**, 81–88 (2004).

30. Liu, K. *et al.* Facile shape-controlled synthesis of luminescent europium benzene-1,3,5-tricarboxylate architectures at room temperature. *CrystEngComm* **11**, 2622–2628 (2009).

31. Seo, Y. K. *et al.* Microwave synthesis of hybrid inorganic–organic materials including porous $Cu_3(BTC)_2$ from Cu(II)-trimesate mixture. *Micropor. Mesopor. Mat.* **119**, 331–337 (2009).

32. Mao, J., Yang, L., Yu, P., Wei, X. & Mao, L. Electrocatalytic four-electron reduction of oxygen with copper (II)-based metal-organic frameworks. *Electrochem. Commun.* **19**, 29–31 (2012).

33. Chui, S. S. A chemically functionalizable nanoporous material $[Cu_3(TMA)_2(H_2O)_3]_n$. *Science* **283**, 1148–1150 (1999).

34. Pech, R. & Pickardt, J. Eatena-Triaqua-lu-[1,3,5-benzenetriearboxylato(2--)]-eopper(lI). *Acta Crystallogr. C* **44**, 992–994 (1988).

35. Deng, S. *et al.* Reduced graphene oxide conjugated Cu_2O nanowire mesocrystals for high-performance NO_2 gas sensor. *J. Am. Chem. Soc.* **134**, 4905–4917 (2012).

36. Zhu, G. *et al.* Facile fabrication and enhanced sensing properties of hierarchically porous CuO architectures. *ACS Appl. Mater. Inter.* **4**, 744–751 (2012).

37. Qiu, M. *et al.* Ultrasound assisted quick synthesis of square-brick-like porous CuO and optical properties. *Mater. Res. Bull.* **47**, 2437–2441 (2012).

38. Zamaro, J. M. *et al.* HKUST-1 MOF: A matrix to synthesize CuO and CuO–CeO$_2$ nanoparticle catalysts for CO oxidation. *Chem. Eng. J.* **195–196**, 180-7 (2012).

39. Liu, B. & Zeng, H. C. Mesoscale organization of CuO nanoribbons: formation of "dandelions". *J. Am. Chem.Soc.* **126**, 8124–8125 (2004).

40. Liu, Y. *et al.* Anion-controlled construction of CuO honeycombs and flowerlike assemblies. *Cryst. Growth Des.* **7**, 467–470 (2007).

41. Qin, Y. *et al.* Hierarchically porous CuO hollow spheres fabricated via a one-pot template-free method for high-performance gas sensors. *J. Phys. Chem. C* **116**, 11994–12000 (2012).

42. Kozhummal, R., Yang, Y., Guder, F., Kucukbayrak, U. M. & Zacharias, M. Antisolvent crystallization approach to construction of CuI superstructures with defined geometries. *ACS Nano* **7**, 2820–2828 (2013).

43. Mao, G., Dong, W., Kurth, D. G. & Möhwald, H. Synthesis of copper sulfide nanorod arrays on molecular templates. *Nano Lett.* **4**, 249–252 (2004).

44. Miles, D. O., Jiang, D., Burrows, A. D., Halls, J. E. & Marken, F. Conformal transformation of [Co(bdc)(DMF)] (Co-MOF-71, bdc = 1,4-benzenedicarboxylate, DMF = N,N-dimethylformamide) into porous electrochemically active cobalt hydroxide. *Electrochem. Commun.* **27**, 9–13 (2013).

45. Zhang, Q., Liu, S.-J. & Yu, S.-H. Recent advances in oriented attachment growth and synthesis of functional materials: concept, evidence, mechanism, and future. *J. Mater. Chem.* **19**, 191–207 (2009).

46. Yuan, Z., Wang, Y. & Qian, Y. A facile room-temperature route to flower-like CuO microspheres with greatly enhanced lithium storage capability. *RSC Adv.* **2**, 8602–8605 (2012).

47. Wang, C., Ye, Y., Tao, B. & Geng, B. Hydrothermal route to twinned-hemisphere-like CuO architectures with selective adsorption performance. *CrystEngComm* **14**, 3677–3683 (2012).

48. Hu, L., Huang, Y., Zhang, F. P. & Chen, Q. W. CuO/Cu$_2$O composite hollow polyhedrons fabricated from metal–organic framework templates for lithium-ion battery anodes with a long cycling life. *Nanoscale* **5**, 4186–4190 (2013).

49. Marioli, J. M. & Kuwana, T. Electrochemical characterization of carbohydrate oxidation at copper electrodes. *Electrochim. Acta* **37**, 1187–1197 (1992).

50. Zhao, J. *et al.* A non-enzymatic glucose sensor based on the composite of cubic Cu nanoparticles and arc-synthesized multi-walled carbon nanotubes. *Biosens. Bioelectron.* **47**, 86–91 (2013).

51. Liu, S. *et al.* A novel non-enzymatic glucose sensor based on NiO hollow spheres. *Electrochim. Acta* **102**, 104–107 (2013).

52. Zhang, Y. W. *et al.* One-pot green synthesis of Ag nanoparticles-graphene nanocomposites and their applications in SERS, H$_2$O$_2$, and glucose sensing. *RSC Adv.* **2**, 538–545 (2012).

53. Tian, J. *et al.* Ultrathin graphitic carbon nitride nanosheets: a low-cost, green, and highly efficient electrocatalyst toward the reduction of hydrogen peroxide and its glucose biosensing application. *Nanoscale* **5**, 8921–8924 (2013).

Acknowledgments

Author contributions

L.W. and Y.S. wrote the main manuscript text. X.L. and J.F. performed the experiments and prepared figures 2–4 and figure 6. C.W. and J.T. prepared figure 1 and figure 5. F.X. and H.T. synthesized the MOFs. Y.S. and J.F. prepared figure 7 and supporting information. All authors reviewed the manuscript.

Additional information